Parametric study of 1D plasma photonic crystals with smooth and discontinuous density profiles^{a)}

W. R. Thomas^{1, b)} and U. Shumlak^{1, c)}

Aerospace and Energetics Research Program, University of Washington,

Seattle, Washington 98195, USA

(Dated: 2 June 2023)

Plasma photonic crystals (PPCs) have the potential to significantly expand the capabilities of current millimeter wave technologies by providing high speed (microsecond time scale) control of energy transmission characteristics in the GHz through low THz range. Furthermore, plasma-based devices can be used in higher power applications than their solid-state counterparts without experiencing significant changes in function or incurring damage. Plasmas with periodic variations in density can be created externally, or result naturally from instabilities or self organization. Due to plasma's diffuse nature, PPCs cannot support rapid changes in density. Despite this fact most theoretical work in PPCs is based on solid-state photonic crystal methods, and assumes constant material properties with abrupt changes at material interfaces. In this work a linear model is derived for a one-dimensional cold-plasma photonic crystal with an arbitrary density profile. The model is validated against a discontinuous Galerkin (DG) method numerical solution of the same device configuration. Bandgap maps are then created from derived group velocity data to elucidate the operating regime of a theoretical PPC device. The bandgap maps are compared for one-dimensional PPCs with both smooth and discontinuous density profiles. This study finds that bandgap behavior is strongly correlated with the density profile Fourier content, and that density profile shapes can be engineered to produce specific transmission characteristics.

^{a)}Published as Physics of Plasmas **30** (6), 063503 (2023). doi.org/10.1063/5.0143827

b) Electronic mail: whitnt@uw.edu.

c)Electronic mail: shumlak@uw.edu.

I. INTRODUCTION

Traditional photonic crystals (PCs) are materials with designer optical properties achieved through the spacing of periodic dielectric or metallic structures. Similar to electrons in a semiconductor lattice, certain energies of photons in a dielectric lattice cannot propagate resulting in energy stop bands, or bandgaps. While the propagation of light in one-dimensional structures has been understood since the late 20th century^{1,2}, engineered two- and three-dimensional, high-contrast materials with complete (omni-directional) bandgaps were first proposed by Yablonovitch³ and John⁴ in 1987. The first complete band gap device was demonstrated for microwaves in 1989 by Yablonovitch *et al.*⁵. Unlike in traditional optics, photons strongly interact with the PC lattice at specific wavelengths, allowing for narrowband devices with a physical size on the order of few wavelengths. As a result, the greatest interest has been in frequency-sensitive applications where space is at a premium, such as sensors⁶, optical data transmission⁷, and optical computing⁸.

Plasma photonic crystals (PPCs) combine the designer optical properties of traditional PCs with the tunability and resistance to high powered electromagnetic radiation of plasmas. First proposed by Hojo and Mase⁹ in 2004 and demonstrated by Sakai *et al.*^{10,11} in 2005, experimental devices include plasma enhanced dielectric or metallic PCs and wave guides^{12–14}, all-plasma PCs with externally imposed order^{10,15,16}, and PCs formed through self-organizing processes^{17–19}. Regular variations in plasma density can also be induced through laser-plasma interactions^{20,21}, and instabilities^{22,23}.

Due to the nature of plasmas, PPCs differ from their solid-state counterparts in several ways. First, the plasma components of a PPC can be created at the time of use and can be tuned on microsecond timescales. Second, once a plasma is fully ionized it will not undergo any further phase change, making PPCs resistant to damage in high power applications. Third, the electron density of atmospheric plasmas $(10^{19}-10^{25}~{\rm m}^{-3})$ implies a target frequency of PPC devices in the GHz to THz range. Finally, plasmas are inherently diffuse. PPCs provide more gradual changes in density compared to the abrupt changes in material properties that occur in solid-state PCs. Many of the proposed PPC devices have density gradient scale lengths that are large compared to the unit spacing. Understanding how these gradients alter transmission properties is essential to predicting PPC behavior.

Several analytical and numerical studies have been undertaken for plasma photonic crystals with non-piecewise constant density profiles. A scattering matrix type method (SMM) was used

to calculate transmission for plasmas with step-function, parabolic, sinusoidal, and Gaussian densities by Lontano and Lunin in 1991^{24,25}. More recently, articles have been published on using the plane wave expansion (PWEM), transmission matrix (TMM), and finite-difference time-domain (FDTD) methods on specific 1D density profiles: sinusoidal²⁶, Gaussian²⁷, exponentially graded^{28,29}, and physically informed density profiles²¹.

In this paper a parametric study of 1D PPCs with smooth and discontinuous density profiles is performed to demonstrate the impact of density gradients on the transmission characteristics. A linear model similar to that used by Lehmann and Spatschek²¹ is outlined for EM waves in an unmagnetized, collisionless, periodically density modulated plasma. A systematic comparison of a smooth density modulated plasma and a discontinuous plasma-vacuum one-dimensional PPC is conducted. The results are validated against discontinuous Galerkin (DG) method numerical solutions of the same configurations. Bandgap maps are then created from derived group velocity data for a range of average plasma frequencies and density modulation amplitudes. The effects of smooth vs discontinuous density profiles on bandgap properties are discussed and the origins of these differences are explored by way of reduced models. This theoretical framework is then used to infer the bandgap characteristics of other types of density profiles. The implications for future PPC devices are discussed.

II. PROPAGATION OF AN EM WAVE IN A COLD, UNMAGNETIZED, 1D PERIODIC PLASMA

In the cold plasma limit, the propagation of weak EM waves through an infinite periodic plasma can be reasonably approximated by Maxwell's equations coupled to the Drude equation^{30,31}, which describes electron motion in a stationary ion lattice (or gas). Solutions to the system can be found through the application of Bloch's theorem³².

In this section the Maxwell-Drude system is solved in a method similar to that described by Lehmann and Spatschek²¹ for a one-dimensional, unmagnetized plasma with an arbitrary periodic density profile. The result is an inhomogeneous wave equation with a source term that depends on the current density j. The equation is linearized in time and space resulting in an infinite set of linear equations coupled through source terms. In order to explore the difference between smooth and discontinuous density profiles, specific solutions are found for two cases: a sinusoidally modulated density profile, and a square wave density profile.

A. The linearized inhomogeneous EM wave equation in an unmagnetized, periodic density modulated plasma in 1D

The behavior of electromagnetic waves in a plasma is governed by Maxwell's equations

$$abla imes oldsymbol{E} = -rac{\partial oldsymbol{B}}{\partial t}, \quad
abla imes oldsymbol{B} = \mu_0 oldsymbol{j} + arepsilon_0 \mu_0 rac{\partial oldsymbol{E}}{\partial t}.$$

$$\nabla \cdot \boldsymbol{E} = \frac{\rho_c}{\varepsilon_0}, \quad \nabla \cdot \boldsymbol{B} = 0. \tag{1}$$

where j is the current density, ρ_c is the charge density, and μ_0 and ε_0 are the vacuum permeability and permittivity, respectively. Faraday's and Ampère's laws can be combined to form an inhomogeneous wave equation for E,

$$\nabla \times \nabla \times \mathbf{E} + \mu_0 \varepsilon_0 \frac{\partial^2 \mathbf{E}}{\partial t^2} = -\mu_0 \frac{\partial \mathbf{j}}{\partial t}.$$
 (2)

The current density j is defined as

$$j = \sum_{\alpha} q_{\alpha} v_{\alpha} n_{\alpha} \tag{3}$$

where α denotes the species. A wave equation can also be found for the magnetic field, \boldsymbol{B} , but has an inhomogeneous part that is a function of $\nabla \times \boldsymbol{j}$. As plasmas used in PPCs are generally cold (< 1 eV), and EM frequencies of interest are well above the typical ion plasma frequency, the time evolution of the plasma current \boldsymbol{j} is assumed to be dictated entirely by electron dynamics, and well approximated by the Drude model^{30,31}

$$\frac{\partial \mathbf{j}}{\partial t} = -\frac{e^2 n(\mathbf{r})}{m_e} \mathbf{E} - \frac{e}{m_e} \mathbf{j} \times \mathbf{B} - \mathbf{v} \mathbf{j}, \tag{4}$$

where e is the electron charge, m_e is the electron mass, v is the collisional relaxation rate, and $n(\mathbf{r})$ is the electron density as a function of space. Written in terms of the electron plasma frequency squared $\omega_{pe}^2 = e^2 n_e / \varepsilon_0 m_e$, and the electron cyclotron frequency $\omega_{ce} = eB_0/m_e$ where B_0 is a constant background magnetic field

$$\frac{\partial \mathbf{j}}{\partial t} = -\varepsilon_0 \omega_{pe}^2(\mathbf{r}) \mathbf{E} - \omega_{ce} \mathbf{j} \times \mathbf{B} / B_0 - \mathbf{v} \mathbf{j}. \tag{5}$$

For the case of an unmagnetized PPC $\omega_{ce} = 0$. To understand the impact of density profile shape as separate from other effects, the collisional relaxation time is assumed to be large relative to the plasma period, i.e. $\omega_{pe} \gg v$. This is not necessarily valid in the case of cold, high density

plasmas like those needed to achieve THz frequencies, therefore the potential consequences of a finite electron-ion collision frequency are discussed in Sec. V.

As a result of the above assumptions, the contribution of the second and third terms in Eq. (5) are negligible. Substituting the Drude equation, Eq. (4), into the wave equation, Eq. (2), results in a final inhomogeneous wave equation that describes temporal and spatial variations of the electric field E for a spatially varying electron density n(r),

$$\nabla \times \nabla \times \mathbf{E} + \mu_0 \varepsilon_0 \frac{\partial^2 \mathbf{E}}{\partial t^2} = \mu_0 \varepsilon_0 \left(\frac{e^2 n(\mathbf{r})}{m_e \varepsilon_0} \right) \mathbf{E}. \tag{6}$$

An arbitrary periodic 1D density profile n(x) is approximated by a Fourier series

$$n(\mathbf{r}) \approx \tilde{n}(x) = n_0 \sum_{\ell} \hat{n}_{\ell} e^{i\ell gx}, \quad \ell \in \mathbb{Z},$$
 (7)

where $n_0 = a^{-1} \int_{-a/2}^{a/2} n(x) dx$ is the average plasma density, $g = 2\pi/a$ is the magnitude of the reciprocal lattice vector, a is the lattice period, and the coefficients \hat{n}_{ℓ} can be found by

$$\hat{n}_0 = \frac{1}{n_0} \left(\frac{1}{a} \int_{-a/2}^{a/2} n(x) dx \right) = 1, \tag{8}$$

$$\hat{n}_{\ell} = \frac{1}{n_0} \left(\frac{1}{a} \int_{-a/2}^{a/2} n(x) e^{i\ell g x} dx \right). \tag{9}$$

As the periodic plasma density is invariant under discrete translation of the primitive lattice vector such that $\tilde{n}(x+ma) = \tilde{n}(x)$, where m is an integer, Bloch's theorem³² states that the solution to the electric field E takes the form of plane waves modulated by a function with the same periodicity as the density. Assuming the electric field is perpendicular to the direction of travel, it can be shown that

$$E(\mathbf{r},t) = \sum_{k} \sum_{\ell} E_{k-\ell g} e^{i((k-\ell g)x - \omega t)} \,\hat{z}, \quad k \in \mathbb{R},$$
(10)

Equations (7) and (10) are combined with the wave equation, Eq. (6), and a Fourier transform is performed in time and space. Rearranging the order of terms for clarity results in a coupled linear system of equations

$$(c_0^2 k^2 - \omega^2 + \omega_{p0}^2) E_k + \omega_{p0}^2 \left(\sum_{\ell=1}^{\infty} \hat{n}_{\ell} E_{k-\ell g} + \sum_{\ell=-1}^{\infty} \hat{n}_{\ell} E_{k-\ell g} \right) = 0,$$
 (11)

where $\omega_{p0} = (e^2 n_0/m_e \varepsilon_0)^{1/2}$ is the electron plasma frequency of the average density, and $c_0 = (\mu_0 \varepsilon_0)^{1/2}$ is the vacuum speed of light. Equation 11 represents an infinite system of equations for each value of k. Note that the first term is the dispersion relation for EM waves in a uniform

plasma with plasma frequency ω_{p0} , while the second is a series of coupling terms with plane waves offset by integer multiples of g and magnitudes proportional to $\omega_{p0}^2 \hat{n}_\ell$. Normalizing Eq. (11) by the lattice frequency, $\omega_a = 2\pi c_0/a$, results in the following non-dimensional expression

$$(K^{2} - \Omega^{2} + \Omega_{p0}^{2}) E_{K} + \Omega_{p0}^{2} \left(\sum_{\ell=1}^{\infty} \hat{n}_{\ell} E_{K-\ell} + \sum_{\ell=-1}^{-\infty} \hat{n}_{\ell} E_{K-\ell} \right) = 0$$
 (12)

where K = k/g is the lattice normalized wavenumber, $\Omega_{p0} = \omega_{p0}/\omega_a$ is the lattice normalized average plasma frequency, and $\Omega = \omega/\omega_a$ is the lattice normalized EM wave frequency. The solution is independent of the magnitude of E_K therefore it will be considered non-dimensional from here forward.

Sections II B and II C explore the form of the coupling terms in Eq. (12) for two density profiles: a sine wave modulation on top of a uniform background density, and a square wave composed of a finite Fourier series.

B. Sinusoidally modulated plasma density

A sinusoidal density modulation is chosen for the smooth PPC case,

$$n(x) = n_0[1 + \chi \sin(gx)], \quad 0 \le \chi \le 1$$
 (13)

where $\chi = (n_{max} - n_0)/n_0$ is the amplitude of the density modulation. Plasmas with a smooth, sinusoidal density profile are likely to occur through laser-plasma interactions^{20,21} or instabilities^{22,23}. This density profile is also a first order Fourier approximation of any periodic profile shape. Fourier coefficients are found by applying Eq. (7) to n(x) in Eq. (13),

$$\hat{n}_0 = 1, \quad \hat{n}_{\pm 1} = \pm \frac{\chi}{2i}.$$
 (14)

Since n(x) is real valued, the Fourier coefficients \hat{n}_{-1} and \hat{n}_{1} are complex conjugates. Substituting the coefficients into the general equation (Eq. (12)) results in the following normalized system of equations for an EM wave in a sinusoidally modulated 1D PPC

$$(K^{2} - \Omega^{2} + \Omega_{p0}^{2})E_{K} + \chi \frac{\Omega_{p0}^{2}}{2i} (E_{K-1} - E_{K+1}) = 0.$$
 (15)

Here a single pair of terms couple E_K to modes E_{K-1} and E_{K+1} . While the quantity of density Fourier coefficients is finite this does not limit the number of coupled equations, only the number of coupling terms. The number of E_K plane waves is still infinite. In order to solve the system numerically the system is truncated based on criteria outlined in Sec. III A.

C. Discontinuous modulated plasma density

The square wave density profile approximates metal-vacuum photonic crystals with their abrupt changes in material properties. It also allows for comparison with existing studies as most assume discontinuous density profiles, despite such profiles being difficult to achieve with plasmas. The density profile has the following form

$$n(x) = \begin{cases} n_0(1+\chi), & a(\ell-1/2) \le x < a\ell \\ n_0(1-\chi), & a\ell \le x < a(\ell+1/2) \end{cases}$$
 (16)

where χ is defined as $\chi = (n_{max} - n_0)/n_0$. Fourier coefficients are found by applying Eq. (7) to n(x),

$$\hat{n}_{\ell} = \frac{\sin \pi \ell}{\pi \ell} + \frac{\chi}{i\pi \ell} (1 - \cos \pi \ell). \tag{17}$$

Written explicitly for terms $|\ell| \le 5$

$$\hat{n}_0 = 1, \quad \hat{n}_{\pm 1} = \pm \frac{2\chi}{i\pi}, \quad \hat{n}_{\pm 2} = 0,$$
 $\hat{n}_{\pm 3} = \pm \frac{2\chi}{i3\pi}, \quad \hat{n}_{\pm 4} = 0, \quad \hat{n}_{\pm 5} = \pm \frac{2\chi}{i5\pi}.$

Note that all even Fourier $(j = \pm 2, \pm 4,...)$ terms are zero. Substituting the Fourier coefficients into Eq. (12) results in the following system for a square density profile approximated by a truncated Fourier series (in this case N = 5)

$$(K^{2} - \Omega^{2} + \Omega_{p0}^{2})E_{K} + \omega_{p0}^{2} \frac{2\chi}{i\pi} \left[(E_{K-1} - E_{K+1}) + \frac{1}{3} (E_{K-3} - E_{K+3}) + \frac{1}{5} (E_{K-5} - E_{K+5}) \right] = 0.$$
(18)

The magnitude of the Fourier coefficients (and therefore the magnitude of the coupling terms) falloff like $1/\ell$. As convergence of the series is slow, even Fourier approximations with large N have significant error. At N=50, the ℓ^2 -norm of the error is still greater than 5%, and does not fall below 1% until N approaches 2000. The effect of Fourier series truncation on bandgap prediction is discussed in Sec. III A.

III. METHOD OF NUMERICAL SOLUTION AND VALIDATION AGAINST WARPXM PLASMA CODE

To solve the linear coupled system described by Eq. (12), it is reformulated as an eigenvalue problem and solved for each wavenumber of interest K. As the number of equations is infinite,

even when the number of density Fourier coefficients is finite, the system must be truncated to be solved numerically. Bounds are set on the minimum convergence of the solution as a function of system size. Band diagrams are constructed by evaluating the system for a range of values of *K*. The band diagram for a discontinuous density profile case is validated against solutions found using a cold plasma model solved with the WARPXM discontinuous Galerkin (DG)^{33,34} code on a Bloch periodic domain³⁵. In order to compare the impacts of smooth vs discontinuous profiles on PPC transmission characteristics, group velocity bandgap maps are constructed from sets of band diagrams where either the density modulation amplitude or lattice normalized electron plasma frequency is varied.

A. Numerical solution of the problem

As developed in Sec. II, the linearized system for an EM wave in plasma with a periodic variation in density consists of an infinite set of coupled equations (Eq. (12)). Reformulated as an eigenvalue problem for Ω^2

$$K^{2}E_{K} + \Omega_{p0}^{2} \sum_{\ell=-N}^{N} \hat{n}_{\ell} E_{K-\ell} = \Omega^{2} E_{K}$$
(19)

or more compactly as

$$AE = \Omega^2 E$$
,

where A is a Hermitian banded matrix, and the eigenvectors E are frequency space solutions of the electric field for each eigenvalue Ω^2 . To truncate the infinite system, a system size limit $M \ge N$ is chosen such that $A \in \mathbb{R}^{(2M+1)\times(2M+1)}$. The matrix A is then expressed in index notation as

$$A_{i=j} = (K+i)^2 + \Omega_{p0}^2, \quad A_{i=j-\ell} = \hat{n}_{\ell} \Omega_{p0}^2,$$
 (20)

where i, j = [-M, M], [-M, M]. The Fourier coefficients \hat{n}_{ℓ} can be found analytically for simple density profiles or numerically for more complex profiles. In index notation the vector E is

$$E_j = E_{K+j}. (21)$$

The system is solved numerically for Ω^2 for a set of K = [0,1]. The square root of the eigenvalues correspond to the frequencies of allowable modes, while the eigenvectors E_K correspond to the wavenumber-space structure of the electric field of each mode. When plotted as a function of K, the frequency corresponding to each eigenvalue form the photonic band structure of the PPC (see

Fig. 1). The spaces between bands where no allowable mode exists for any value of K are known as bandgaps or forbidden regions.

To ensure that the truncated system is fully converged, a method of determining the minimum acceptable value of M is required. The error increases with increasing band number for truncated systems. In this work, the region of interest is confined to the first eight bands, which sets a lower bound on M. Sufficient convergence is defined as the minimum value of M such that the l^2 -norm of the normalized difference between the M and M-1 solution for the eighth band is less than 10^{-6} , or

$$||\Delta\Omega_{8,M}||_2 = \sqrt{\frac{\sum_K |\Omega_{8,M} - \Omega_{8,M-1}|^2}{\sum_K |\Omega_{8,M}|^2}} < 10^{-6}.$$
 (22)

B. Validation of the analytical model with a nonlinear plasma model solved using the WARPXM code

WARPXM, an unstructured discontinuous Galerkin multi-physics plasma code developed at the University of Washington³⁴, is used to evaluate the equivalent problem as a system of normalized hyperbolic PDEs

$$\frac{\partial \boldsymbol{p}_e}{\partial t} = \left(\frac{L}{\delta_p}\right) \left(\frac{1}{A_e}\right) \boldsymbol{p}_e \times \boldsymbol{B},\tag{23}$$

$$\frac{\partial \mathbf{E}}{\partial t} = (\omega_p \tau)^2 \left[\left(\frac{\delta_p}{L} \right)^2 \nabla \times \mathbf{B} - \left(\frac{\delta_p}{L} \right) \left(\frac{1}{A_e} \right) \mathbf{p}_e \right], \tag{24}$$

$$\frac{\partial \boldsymbol{B}}{\partial t} = -\nabla \times \boldsymbol{E},\tag{25}$$

where p, E, B, and t are normalized by reference values $p_0 = m_p n_0 c_0$, $E_0 = c_0 B_0$, $B_0 = (\mu_0 m_p n_0 c_0^2)^{1/2}$, and $\tau = L/c_0$, respectively. The reference density, n_0 , is chosen based on typical density values, L is the problem length scale, m_p is the proton mass, and c_0 is the vacuum speed of light. The nondimentional parameters are: δ_p/L , the normalized proton skin depth, $A_e = m_e/m_p$, the proton normalized electron mass, and $\omega_p \tau$, the normalized proton plasma frequency. Ions are assumed stationary to be consistent with the analytical model described in Sec. II.

The WARPXM code computes the evolution of the electron momentum and electric and magnetic fields by solving Eqs. (23)-(25). A solution is initialized that describes a propagating TE, TM, or TEM wave. To simulate an infinitely periodic system, Bloch boundary conditions³⁵ are implemented. The WARPXM code applies boundary conditions by setting the value of virtual

nodes at the boundaries. The left and right virtual boundary nodes, q_R^v and q_L^v respectively, are functions of the opposite boundary node value, q_L and q_R , and a phase shift, ψ ,

$$q_R^{\nu} = q_L e^{-i\psi},\tag{26}$$

$$q_L^{\nu} = q_R e^{i\Psi},\tag{27}$$

where $\psi = ka$, and *i* here denotes the unit imaginary number. The boundary conditions allow for the representation of an infinite periodic plasma with period *a*, while permitting EM waves with wavenumbers other than integer multiples of the inverse domain length. Simulations are performed for each *k* value of interest. Note that real and imaginary components of the electric and magnetic fields are needed for the Bloch boundary conditions, so Eqs. (23)-(25) are complex-valued equations.

Electric and magnetic field values are sampled at regular time intervals for several points in the domain that do not fall on any axis of symmetry. This sampling strategy mitigates inadvertently sampling values at or near field nulls which could lead to weak detection of particular modes. A fast Fourier transform (FFT) algorithm is then applied to the data, and the spectra are averaged over all sampled points.

Band diagrams are assembled by running simulations with different wavenumbers k in the range of interest. Plotting the logarithm of the spectral intensity produces the band diagram from the nonlinear plasma simulations, as is shown in Fig. 1, using the real component of the electric field. The band diagram using the imaginary component gives a similar result. A total of 41 simulations, each with a different value of k, adequately resolve the wavenumber space. Simulations to generate a complete band diagram take approximately five hours using a single core on a modest workstation.

The analytical and numerical band diagrams are compared for each band and the l^2 -norm of the relative difference is calculated for each band i

$$||\Delta\Omega^{i}||_{2} = \sqrt{\frac{\sum_{k} |\Omega_{anal}^{i} - \Omega_{num}^{i}|^{2}}{\sum_{k} |\Omega_{anal}^{i}|^{2}}}.$$
(28)

Calculated errors for five different density profile cases are shown in Table I. In all cases there is good agreement as the error is on the order of the frequency resolution of the simulation. Large plasma frequencies to lattice frequency ratios Ω_{p0} , and square density profiles generally produce larger errors. This is also reflected in the increase in system size needed to sufficiently resolve the problem.

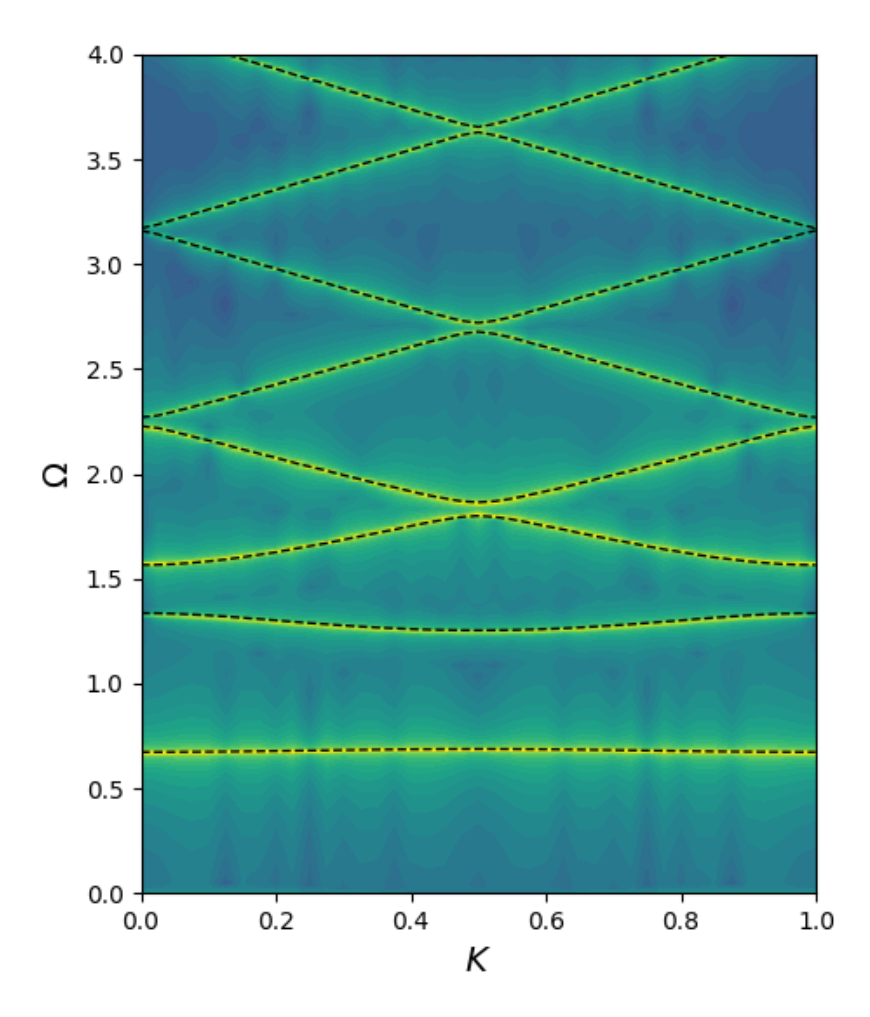


FIG. 1. Comparison of band diagrams generated by solving the nonlinear plasma system, Eqs. (23)-(25), using WARPXM (color contours indicate magnitude of spectra) and the analytical model described in Sec. II (dashed lines) for a square plasma density profile with $\Omega_{p0} = 1$ and $\chi = (n_{max} - n_{avg})/n_{avg} = 1$.

C. Construction of velocity bandgap maps

One of the key advantages of plasma photonic crystals over solid-state PCs is their tunability. Where parametric studies are useful for device design in dielectric or metal PCs, for PPCs they can also be used to describe the operational regime of a single device. As the bandgap is generally the most important characteristics of a PC, bandgap maps³⁶ are a convenient representation of a PC's performance.

In solid-state PCs, the unitless design parameters most used are the dielectric contrast, ε_{high} :

TABLE I. The l^2 -norm of the relative difference between the analytical and WARPXM results for the first five bands, $||\Delta\Omega^i||_2$ (see Eq. (28)). In all cases the absolute difference is on the order of the simulation frequency resolution, $\omega_{res}/\omega_a = a/c_0T = 0.25 \times 10^{-2}$, where T is the simulation total run time. System size is chosen by the condition in Eq. (22).

		Solution difference, $ \Delta\Omega^i _2 \times 10^{-2}$				
Density profile	System Size	Band 1	Band 2	Band 3	Band 4	Band 5
Sine ^a , $\Omega_{p0} = 0.5$	13×13	0.30	0.31	0.13	0.10	0.06
Sine, $\Omega_{p0} = 1.0$	13×13	0.39	0.25	0.16	0.08	0.07
Sine, $\Omega_{p0} = 2.0$	17×17	0.87	0.36	0.05	0.12	0.09
Square ^b , $\Omega_{p0} = 1.0$	21×21	0.60	0.94	0.07	0.09	0.05
Square, $\Omega_{p0} = 2.0$	25×25	0.76	0.77	1.18	0.20	0.41

^a See Section II B for sinusoidally modulated density profile parameters.

 ε_{low} , and the fill fraction $f=d_{high}/a$, where d_{high} is the width of high dielectric constant layer, and a is the lattice spacing. In PPCs the plasma density is most often the easiest and fastest tunable parameter, whereas fill fraction is either fixed or a secondary effect that is not easy to control independently of plasma density. For the study of PPCs, the primary unitless parameters of interest are chosen to be density modulation amplitude, $\chi=(n_{max}-n_{avg})/n_{avg}$, and the lattice normalized electron plasma frequency of the average density, $\Omega_{p0}=\omega_{pe0}/\omega_a$.

Photonic crystal bandgap maps are traditionally formed by plotting bandgap edges as a function of either fill fraction or dielectric contrast. Bandgap edges can be found either through dispersion data³⁶ or transmission spectra³⁷, though density of states contours have also been used^{38,39}. In this work, bandgap maps are created by calculating the group velocity for individual bands, which has the added benefit of including more useful information on transmission properties around the bandgap edges.

Bandgap maps are generated by calculating a series of band diagrams (as in Fig. 2), with each band diagram changing the parameter of choice by some small amount. Each bandgap map presented in Sec. IV is constructed from 200 band diagrams. Group velocity, $v_g = \partial \Omega / \partial K$, is found by calculating the slope at each value of K from 0 to 1/2 using the central difference operator for interior K values and one-sided difference operators at the boundaries. The calculated slopes

^b See Section II C for piecewise constant density profile parameters.

are binned by frequency Ω . In forbidden regions where no slope exists the bin is assigned to NaN. Group velocities are normalized to the speed of light and plotted as color contours, and bandgaps appear as blank spaces, as seen in Figs. 3-5.

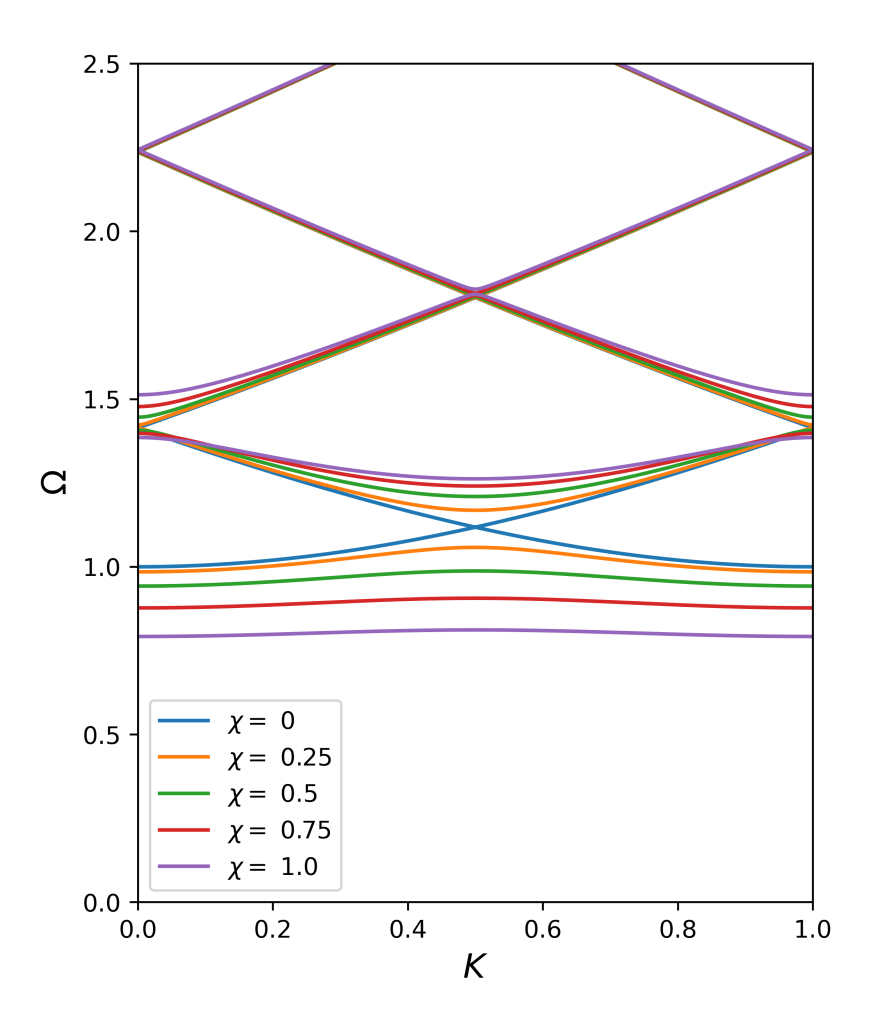


FIG. 2. Band diagram for a sinusoidally modulated density profile with lattice averaged plasma frequency $\Omega_{p0} = 1$ and modulation amplitude varying from $\chi = 0 - 1$.

IV. BANDGAP MAP COMPARISON OF SMOOTH AND DISCONTINUOUS DENSITY PROFILES

Group velocity bandgap maps are created for the smooth and discontinuous density profiles using the procedures described in Sec. III. The area of interest is confined to lattice normalized

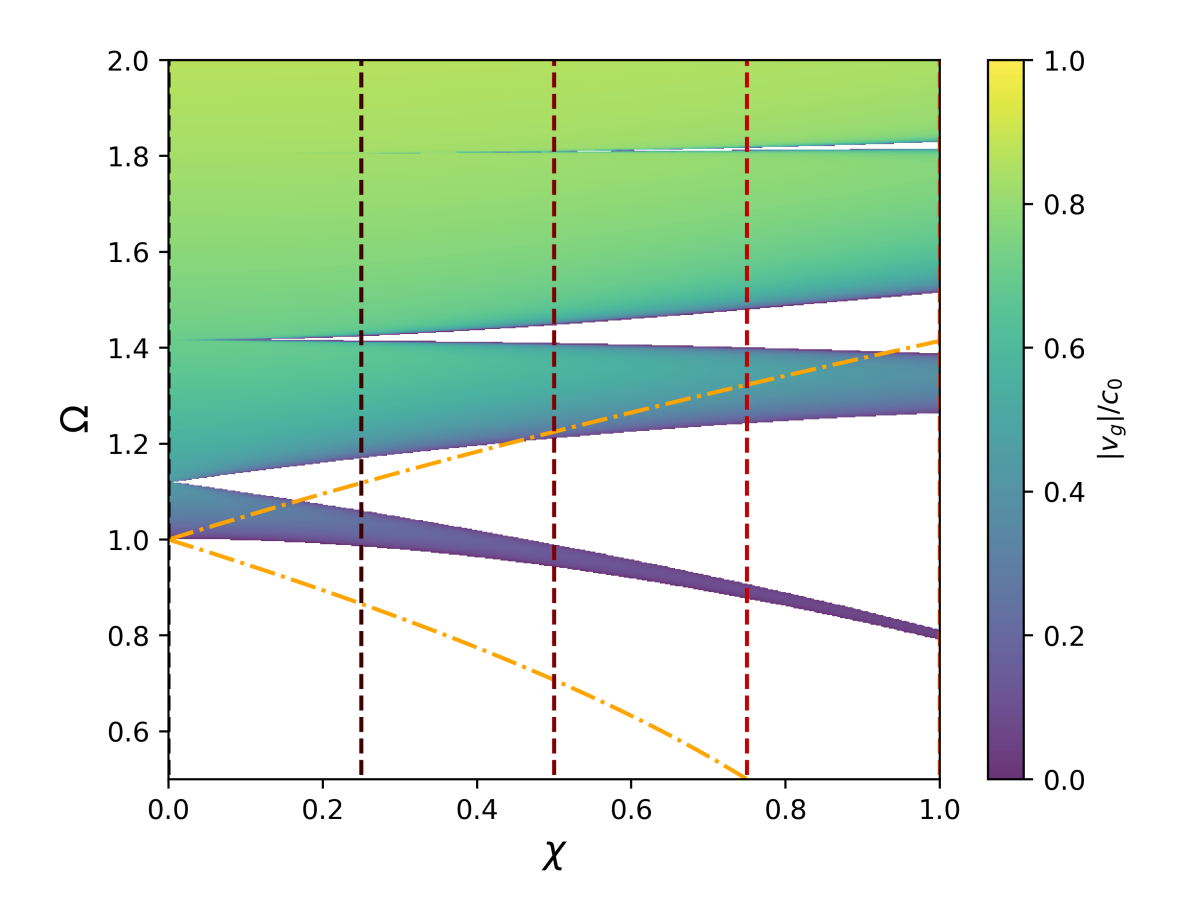


FIG. 3. Contours of group velocity for a smooth, sinusoidally modulated density profile with modulation amplitudes varying from 0 to 1. The plot provides a bandgap map, which facilitates interpretation of the effects of modulation amplitude on bandgaps. Normalized average plasma frequency $\Omega_{p0} = 1$ for all cases. Vertical dashed lines indicate locations of band diagrams in Fig. 2 at K = 0.25, 0.5, and 0.75 respectively, and orange dashed-dotted lines indicate locations of plasma frequencies at minimum and maximum densities. Bandgaps extend well beyond the maximum plasma frequency.

average density plasma frequencies between $\Omega_{p0} = 0 - 3$ and lattice normalized EM wave frequencies of $\Omega = 0 - 4$, as this region is sufficient for capturing the dominate bandgap features. In this section, the smooth, sinusoidally modulated density profile is explored by varying both χ and Ω_{p0} . The smooth density profile bandgap maps are then contrasted with the bandgap maps of the discontinuous density profile. The origins of these differences are explored in Sec. V.

A. Smooth density profile

By plotting contours of the group velocity for a sinusoidally modulated density profile with modulation amplitudes varying from $\chi=0$ to 1, and $\Omega_{p0}=1$, a bandgap map is produced in Fig. 3 that facilitates understanding of the impact of modulation amplitude on photonic bands. The blank contour indicates the absence of bands, or bandgaps. The left boundary of the plot, at $\chi=0$, represents the dispersion of a uniform plasma. The orange dash-dot lines represent the plasma frequency of the maximum and minimum density regions, respectively. As the modulation amplitude increases, the first bandgap appears just above the plasma frequency at $\Omega\approx 1.1$. A second and third bandgap appear by $\chi=0.5$, at $\Omega\approx 1.4$ and 1.8 respectively. At $\chi=1$ the dispersion of the density modulated plasma has deviated significantly from the dispersion of a uniform plasma ($\chi=0$). Note that all bandgaps begin above the plasma frequency of the maximum density.

The gap map in Fig. 4 shows the effect of varying the plasma frequency of the average density Ω_{p0} , for two density profiles. Color contours indicate a sinusoidally modulated density profile with a maximum modulation amplitude ($\chi = 1$) and gray shading indicates a uniform plasma ($\chi = 0$) with the same Ω_{p0} . The orange dashed-dotted line in Fig. 4 indicates the plasma frequency of the maximum density for the sinusoidally modulated density profile. The minimum density and plasma frequency are zero for all cases.

Several differences between the density modulated and uniform plasma profiles can be readily identified. Despite having the same average plasma frequency, forbidden regions in the density modulated case extend above not only the average plasma frequency, but also above the plasma frequency of the maximum density (upper orange dashed-dotted line). The bandgap map provides clues to the origin of individual bandgaps: when extrapolated to the left axis, each bandgap can be seen to start at half lattice frequency intervals, corresponding to band diagram intersections at K=0 and 0.5. These bandgaps continue for EM wave frequencies many times the lattice frequency.

B. Discontinuous density profile

The dispersion of a discontinuous and smooth density profile are compared in the bandgap map in Fig. 5. The discontinuous density profile gap map (color contours) is overlayed on the smooth

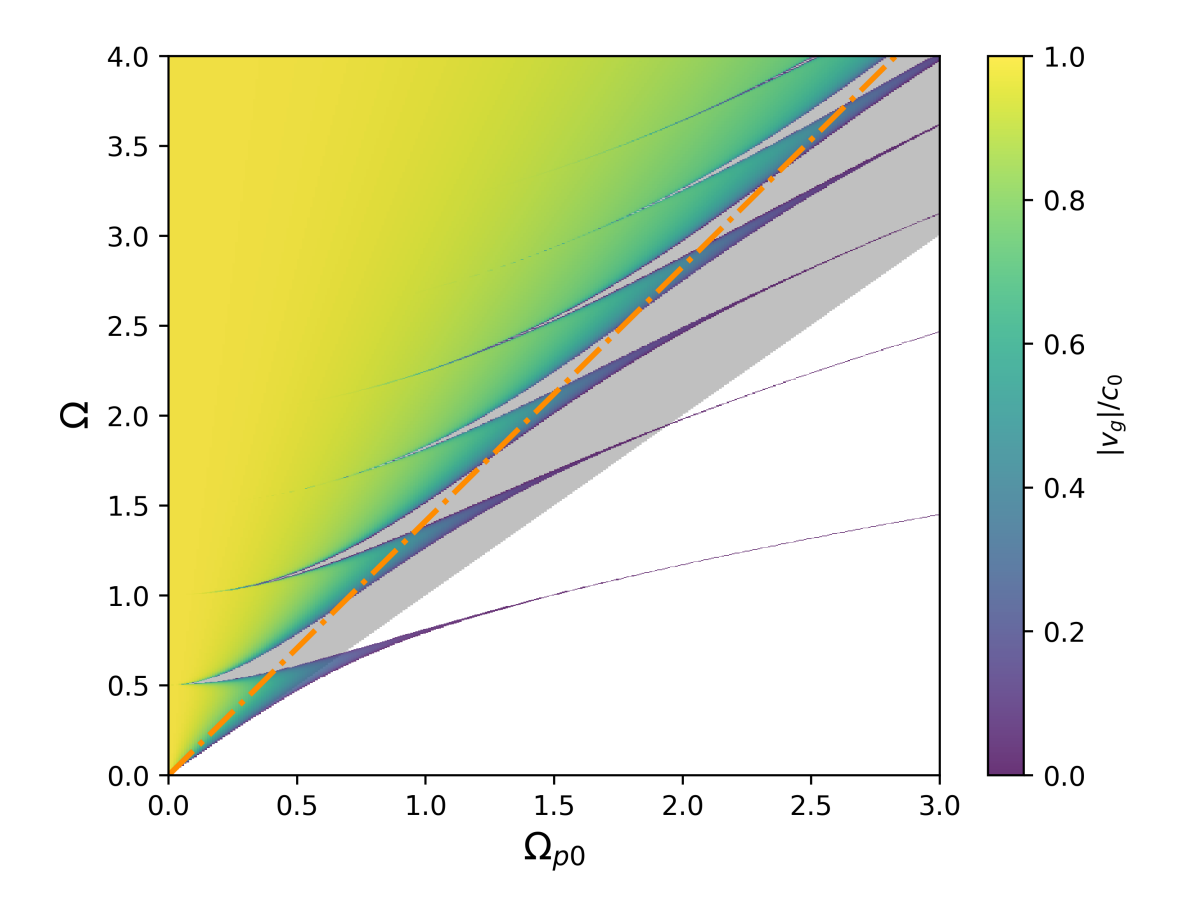


FIG. 4. Contours of group velocity as a function of the plasma frequency of the average density Ω_{p0} for a sinusoidally modulated (color contours) and uniform plasma (gray contours), or $\chi=1$ and $\chi=0$, respectively. The color bar indicates group velocity normalized by c_0 . Plasma frequency of the maximum density for the sinusoidally modulated plasma is indicated by the dashed-dotted orange line. Bandgaps for the sinusoidally modulated plasma extend well above the maximum plasma frequency.

density profile gap map from Fig. 4 (gray shading). Both profiles have the same modulation amplitude $\chi=1$ and a filling fraction of $f=d_{plasma}/a=0.5$, corresponding to equal width regions of low and high density.

There are notable similarities between the bandgap maps for both cases. The same number of bandgaps are present in both the discontinuous and smooth cases, and the bandgaps begin at similar frequencies. In fact, the first bandgap, beginning at $\Omega=0.5$, is almost identical for $\Omega_{p0}\leq0.5$.

Despite the bandgap maps for the discontinuous and smooth density profiles having a similar general structure, major difference are evident. The first significant difference is the appearance

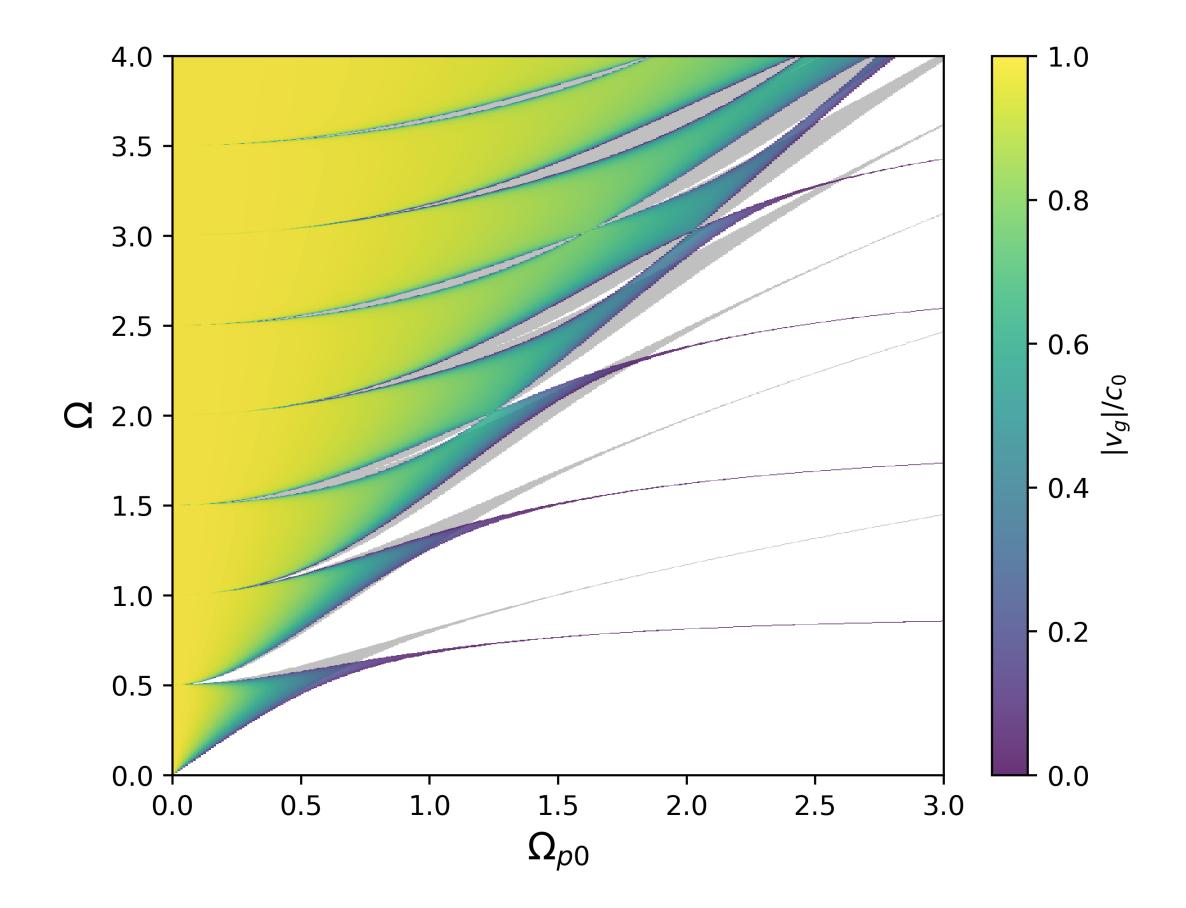


FIG. 5. Contours of group velocity for a discontinuous and smooth density profile. The discontinuous density profile gap map (color contours) is overlayed on the smooth density profile gap map from Fig. 4 (gray shading). Both profiles have the same modulation amplitude $\chi = 1$ and a filling fraction of $f = d_{plasma}/a = 0.5$. The plasma frequency of the average density, Ω_{p0} , is shown in the x-axis. Contour colors indicate group velocity normalized by c_0 . The bandgap maps for discontinuous and smooth density profiles differ significantly.

of forbidden islands in the discontinuous case at large Ω . The origin of these islands will be explored in Sec. V. Furthermore, the forbidden islands alternate in size and extent, whereas the bandgaps in the smooth density profile case all have a similar size and shape. The second major difference are the widths and central frequencies of bandgaps at large Ω_{p0} . While the bandgaps for the smooth density profile continue to increase in Ω with increasing Ω_{p0} , the bandgaps for the discontinuous profile appear to asymptote. This can be explained by understanding that the narrow bands between bandgaps at large Ω_{p0} correspond to stationary modes trapped in density troughs.

Similar to an electron in a potential well, the frequency of the trapped modes is a strong function of potential well shape. Rectangular potential wells have stationary mode frequencies independent of potential well depth beyond a minimum. In contrast, the sides of shaped wells steepen with increasing depth, causing trapped mode frequencies to change.

Just as the smoothly modulated plasma is not well approximated by a homogeneous plasma of the same average density, the discontinuous density profile plasma is not well approximated by a smoothly modulated plasma with the same minimum and maximum densities. This is especially true at higher frequencies. In Sec. V, the origins of these differences is explored.

V. UNDERSTANDING THE ORIGINS OF BANDGAPS THROUGH REDUCED MODELS

Many of the differences between the bandgap characteristics of the smooth and discontinuous density profiles can be explored through studying the interaction of a subset of electromagnetic wave modes. In this section, two types of reduced models are explored. First (see Sec. V A), a two-mode reduced model is used to derive an analytical approximation of the width of arbitrary bandgaps, as well as generate band diagrams and bandgap maps that are compared to the full model. While the two-mode reduced model captures primary interactions between individual wave modes, higher-order interactions can also be significant. In Sec. V B, three- and seven-mode reduced models are used to generate bandgap maps in order to highlight the contribution of higher-order coupling terms.

A. Two-mode reduced model

The two-mode reduced model is a truncation of the infinite system in Eq. (12) to only two waves: E_K and E_{K-j} , where $j \ge 1$ and indicates the number of the bandgap of interest. Note that a value of j > 1 indicates that the two modes are nonconsecutive. All other modes are set to zero, reducing the system to two coupled equations

$$(K^{2} - \Omega^{2} + \Omega_{p0}^{2}) E_{K} + \hat{n}_{j} \Omega_{p0}^{2} E_{K-j} = 0,$$

$$((K - j)^{2} - \Omega^{2} + \Omega_{p0}^{2}) E_{K-j} - \hat{n}_{-j} \Omega_{p0}^{2} E_{K} = 0.$$
(29)

In the case of a uniform plasma, $\hat{n}_j = \hat{n}_{-j} = 0$, the equations become decoupled (see the blue line in Fig. 6). The first equation is the dispersion relation for EM waves traveling in a cold,

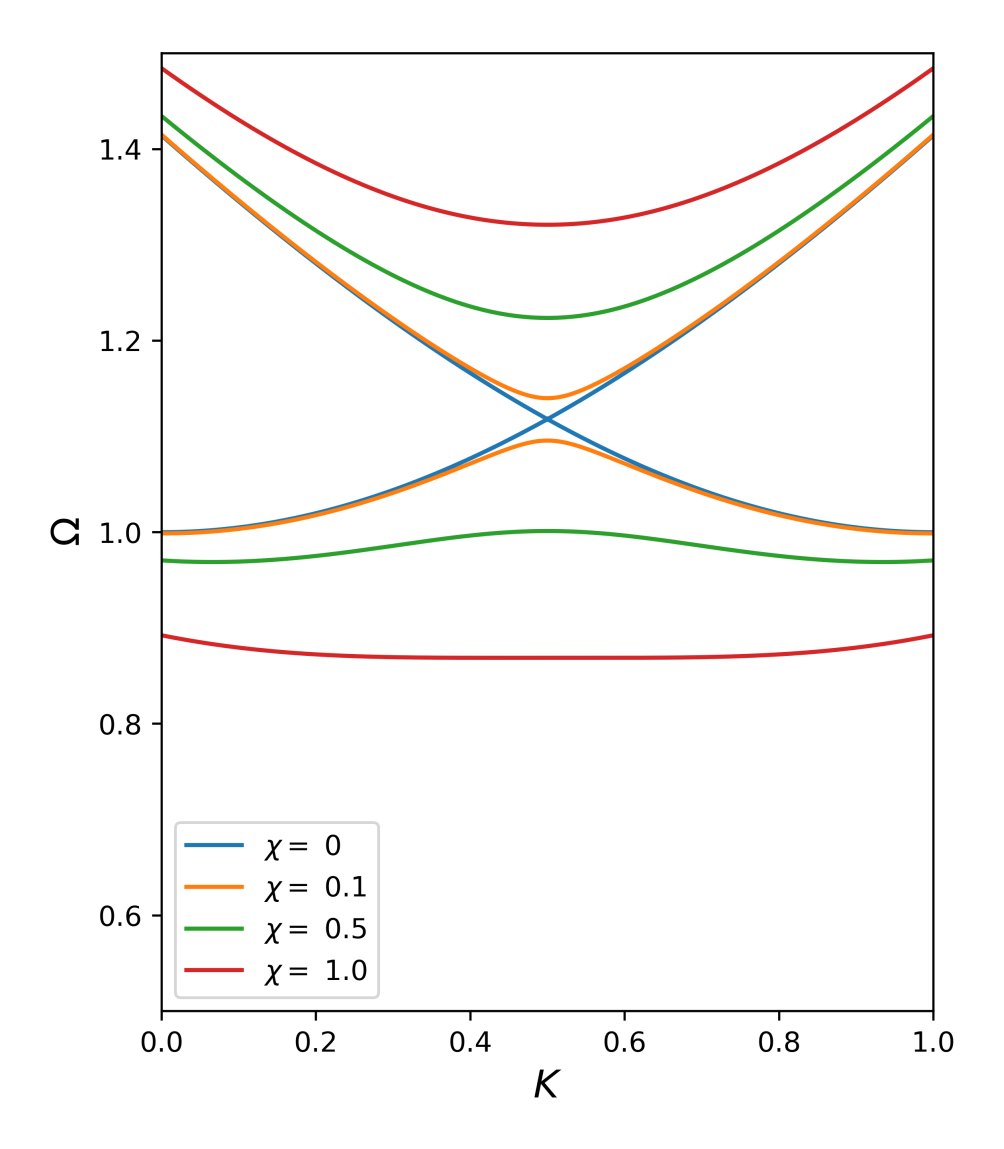


FIG. 6. Band diagram given by the two-mode reduced model for a uniform plasma (blue) and sinusoidally modulated plasma with modulation amplitudes of $\chi=0.1$ (orange), $\chi=0.5$ (green) and $\chi=1$ (red). Lattice normalized plasma frequency of $\Omega_{p0}=1$ for all cases. Increased density modulation amplitude leads to increased mode coupling around the band intersection at K=0.5, generating, and then expanding the bandgap at $\Omega\approx 1.1$.

homogeneous plasma. The second is the same dispersion relation, shifted in K by j. The two dispersion relations intersect at K = j/2 where the E_K wave has a positive group velocity, and the E_{K-j} wave's group velocity is negative. The two waves are counter propagating, but not interacting.

For non-zero values of $\hat{n}_{\pm j}$, the system is coupled and the counter propagating waves begin to interact. In Fig. 6, the orange, green, and red lines show the two-mode reduced model solution for $\chi = 0.1$, 0.5 and 1, respectively. Even at small modulation amplitude coupling between forward and backward propagating modes leads to a bandgap in the vicinity of the band intersection. Physically, this translates to reflection of all frequencies within the bandgap. With increasing modulation amplitude this reflection band increases dramatically, and distorts the two original bands from the unmodulated case.

The system in Eq. (29) can be analytically solved for Ω . Using the fact that \hat{n}_{-j} is the complex conjugate of \hat{n}_{+j} , the positive values of Ω are

$$\Omega_{\pm j}(K) = \left\{ \Omega_{p0}^2 + j^2/2 - jK + K^2 \pm \frac{1}{2} \left[j^2 (j - 2K)^2 - 4|\hat{n}_j|^2 \Omega_{p0}^4 \right]^{1/2} \right\}^{1/2},$$
(30)

where $\Omega_{+j}(K)$ and $\Omega_{-j}(K)$ indicate the normalized frequency of the upper and lower positive bands, respectively, for a system with a given j, as a function of normalized wavenumber K. Bandgap edges can be inferred from band frequencies at symmetry points K = 0 and 1/2. The lower and upper edges of the bandgap are the maximum value of the lower band and minimum value of the upper band, respectively,

$$\Omega_{-j,BG} = \max(\Omega_{-j}(0), \ \Omega_{-j}(1/2)),
\Omega_{+j,BG} = \min(\Omega_{+j}(0), \ \Omega_{+j}(1/2)).$$
(31)

The bandgap edges are well approximated by the band frequencies at K = 1/2,

$$\Omega_{\pm j,BG} \approx \Omega_{\pm j}(1/2) = \sqrt{\Omega_{p0}^2(1 \pm |\hat{n}_j|) - (j/2)^2},$$
(32)

which indicates that each bandgap j is a function of Ω_{p0} and the magnitude of the jth density Fourier coefficient, $|\hat{n}_j|$. Similarly, the upper bound of the cutoff region is well approximated by the minimum of the lower band for the j = 1 case at K = 0

$$\Omega_{CO} \approx \Omega_{-1}(0) = \frac{1}{\sqrt{2}} \sqrt{1 + 2\Omega_{p0}^2 - \sqrt{1 - 4|\hat{n}_1|^2 \Omega_{p0}^4}}.$$
 (33)

which reduces to Ω_{p0} as the density modulation amplitude decreases $(|\hat{n}_1| \to 0)$.

In Fig. 7, the two-mode reduced model predictions of the cutoff region (blue) and bandgaps (orange) for the smooth density profile are compared against full model (gray). At low normalized

plasma frequencies, Ω_{p0} < 0.5, the two solutions are very similar, indicating two-mode wave coupling is dominant in this region.

As the lattice normalized plasma frequency increases, the solutions increasingly diverge. Not only does the reduced model overpredict the width and average frequency of bandgaps at these higher frequencies, but it fails to predict higher bandgaps entirely. This can be understood from the dependence of Eq. (32) on $|\hat{n}_j|$. The sinusoidally modulated case only has non-zero values for $\hat{n}_{\pm 1}$, resulting in the reduced model predicting only one bandgap. In reality, more than two modes are present and interact through higher-order coupling. In the bandgap map, this higher-order coupling appears as harmonics of the first bandgap repeated at integer multiples of half the lattice frequency $\Omega_a/2$.

Figure 8 compares the two-mode reduced model to the full model for the discontinuous density profile. In contrast to the smooth density profile case, some (but not all) of the higher bandgaps are predicted by the reduced model. This is expected as the discontinuous density profile has non-zero density Fourier coefficients for odd values of j; therefore, the reduced model predicts finite odd bandgaps.

The reduced model again well approximates the full model for smaller values of Ω_{p0} , but diverges with increasing Ω_{p0} . Also like the smooth density profile case, not all bandgaps are predicted by the reduced model. These unpredicted bandgaps are all even (bandgaps 2, 4, and 6 in Fig. 8), and are distinguishable from the predicted bandgaps by beginning later, at higher values of Ω_{p0} . Again, these unpredicted bandgaps can be understood as harmonics that results from higher-order coupling.

The most prominent difference between the smooth and discontinuous profile bandgap maps, the forbidden islands, is not predicted by the two-mode reduced model. Therefore the bandgap islands appear to be the result of interactions between first-order mode coupling and higher-order harmonics. In Sec. V B, reduced models with additional modes are used to explore the origin of forbidden islands.

B. Three- and seven-mode reduced models

The interaction of pairs of electromagnetic modes has been shown in Sec. V A to describe many of the dominant features of bandgap behavior, such as the cutoff region and bandgaps associated with non-zero density Fourier coefficients. The two-mode reduced model is not able to capture

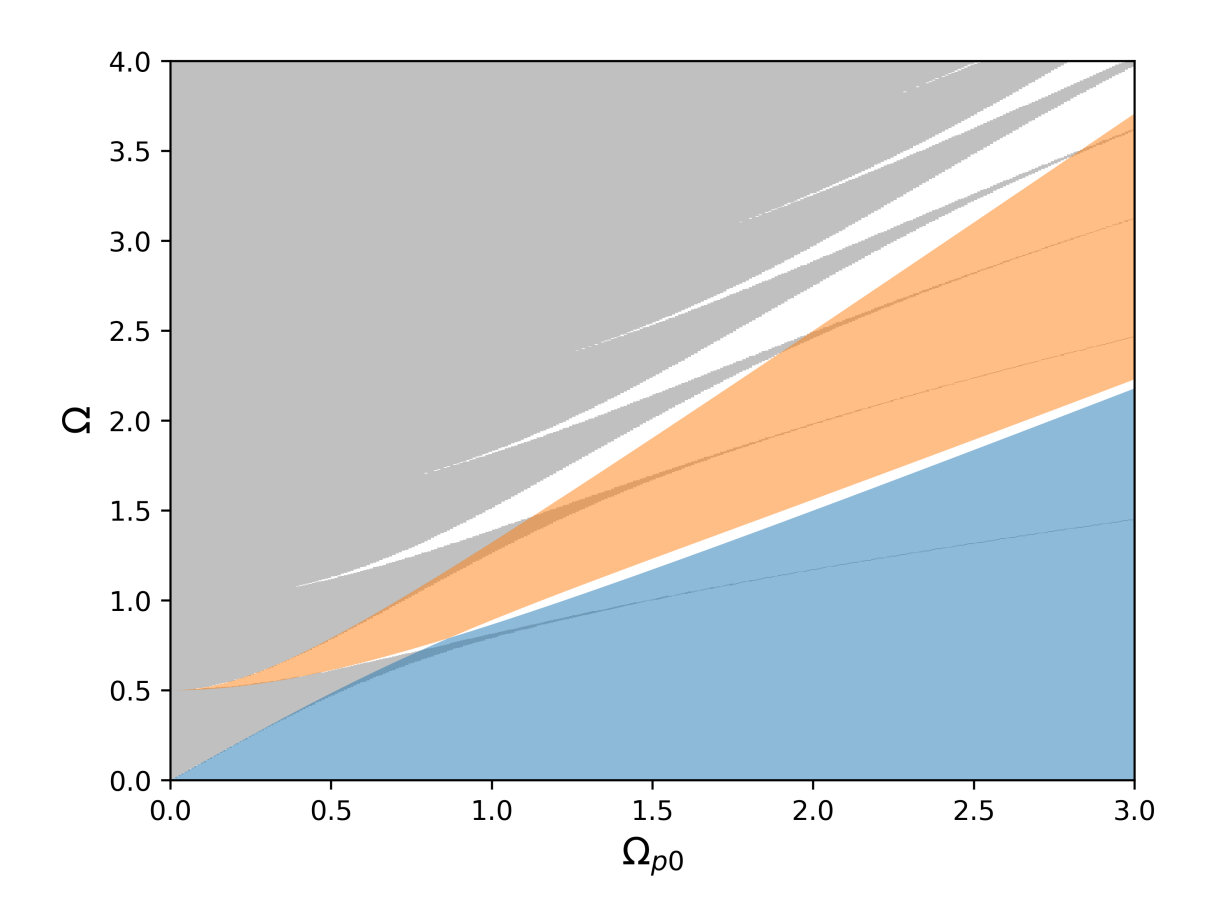


FIG. 7. The smooth density profile gap map (gray) is overlaid with predictions by the two-mode reduced model for the cutoff region (blue) and first bandgap (orange). Models agree well for $\Omega_{p0} < 0.5$, but depart with increasing Ω_{p0} . Higher bandgaps are not predicted by the reduced model as they result from higher-order coupling effects.

bandgaps not associated with non-zero density coefficients, bandgap widths at large Ω_{p0} , or forbidden islands in the discontinuous density case. In order to elucidated the origins of these other features, reduced models with three and seven consecutive modes are used to produce bandgap maps. In contrast to the two-mode reduced model, the systems are all Hermitian and are solved using the method described in Sec. III A. A greater span of reduced models is explored in this work, but the three-mode and seven-mode reduced models best elucidate the features of the smooth and discontinuous density profiles, respectively.

In Fig. 9, bandgaps are calculated with the three-mode reduced model for the sinusoidally modulated density case. When compared to the results for the two-mode reduced model in Fig. 7,

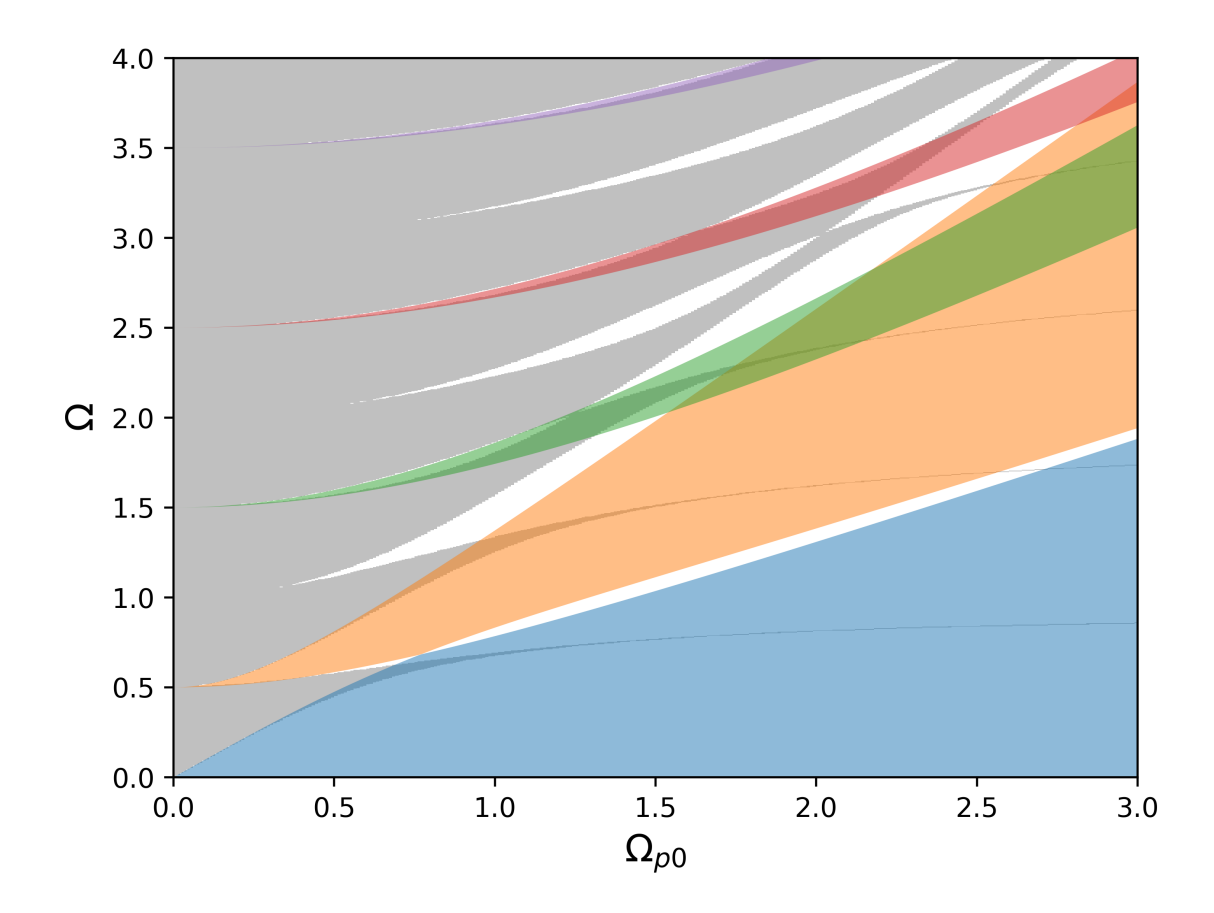


FIG. 8. Discontinuous density profile gap map (gray) is overlaid with predictions by the two-mode reduced model. This includes the cutoff region (blue), and the first (orange), third (green), fifth (red), and seventh (purple) bandgaps. As in the smooth density profile case, models agree well only for $\Omega_{p0} < 0.5$. The formation of forbidden islands in the bandgap map is not predicted by the reduced model, and is a result of the interaction of three or more modes. The even-numbered bandgaps are also not predicted as they result from higher-order coupling effects not captured by the reduced model.

the cutoff (blue) and first bandgap (orange) more closely approximate the full model. Additionally, higher-order coupling results in a second bandgap (green). As the size of the reduced model is increased, additional bandgaps appear, one for each additional mode (not shown).

Figure 10 compares the bandgap map from the full model (gray) with bandgaps predicted by the seven-mode reduced model. In contrast to the two-mode reduced model in Fig. 8, even bandgaps are present, and the odd bandgaps are less prominent. Another significant difference is the appearance of forbidden islands in bandgaps three (red) and four (purple). Seven modes are found to

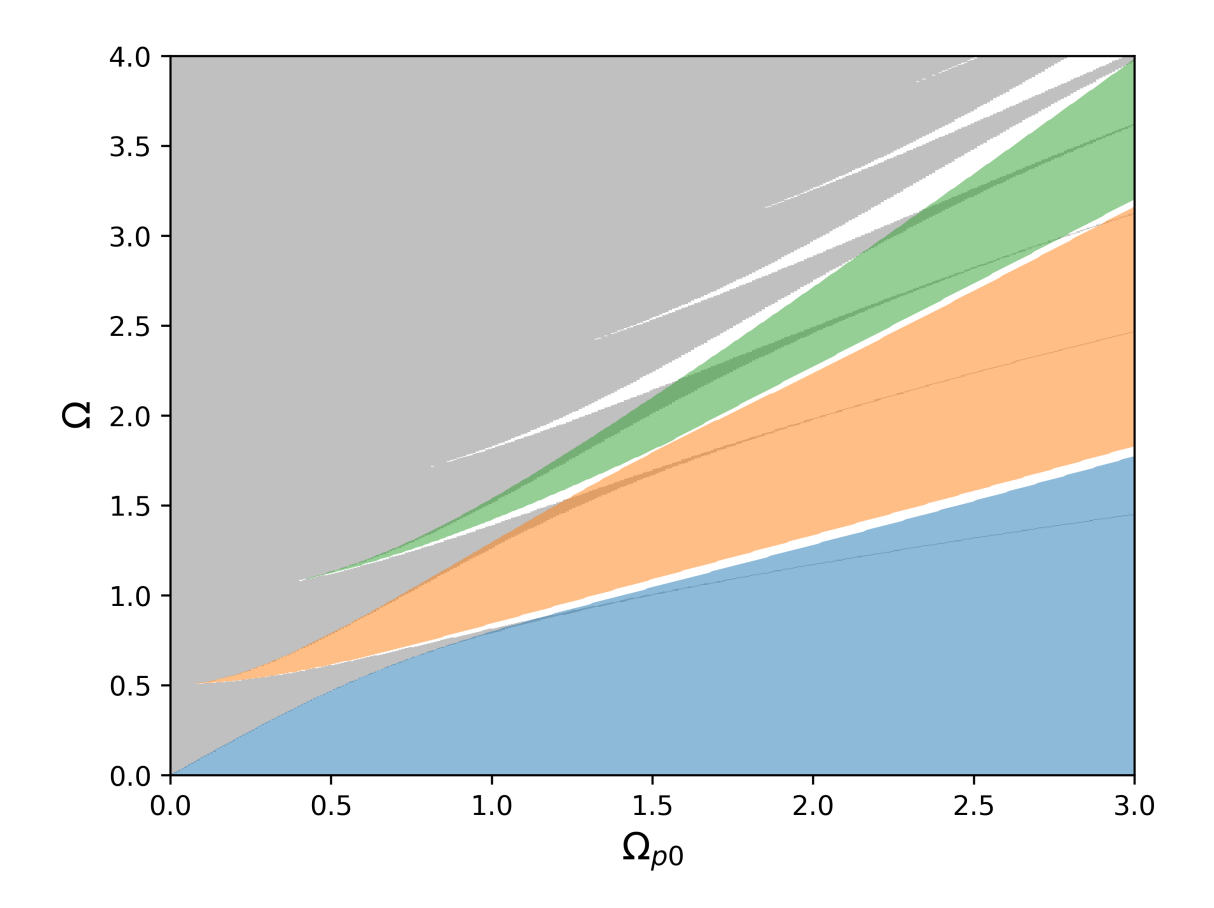


FIG. 9. The smooth density profile gap map (gray) is overlaid with predictions by the three-mode reduced model for the cutoff region (blue), and bandgaps (orange and green). When compared to the two-mode reduced model in Fig. 7, the three-mode model more closely approximates the cutoff and first bandgap in the full model. Additionally, higher-order coupling results in a second bandgap (green).

be the minimum number needed to resolve any forbidden islands, as well as finite density Fourier coefficients at $|\ell|=3$, where ℓ is the density Fourier coefficient index (see Eq. (17)). Interestingly, when density profiles have both even and odd non-zero density Fourier content (such as Gaussian or saw-tooth profiles) no forbidden islands are formed. Forbidden islands are therefore sensitive to the details of the Fourier content of the PPC's density profile.

VI. DISCUSSION

The sinusoidally modulated and discontinuous density profiles represent useful limits of possible density profiles. Many proposed PPC devices include both gradual changes in density and

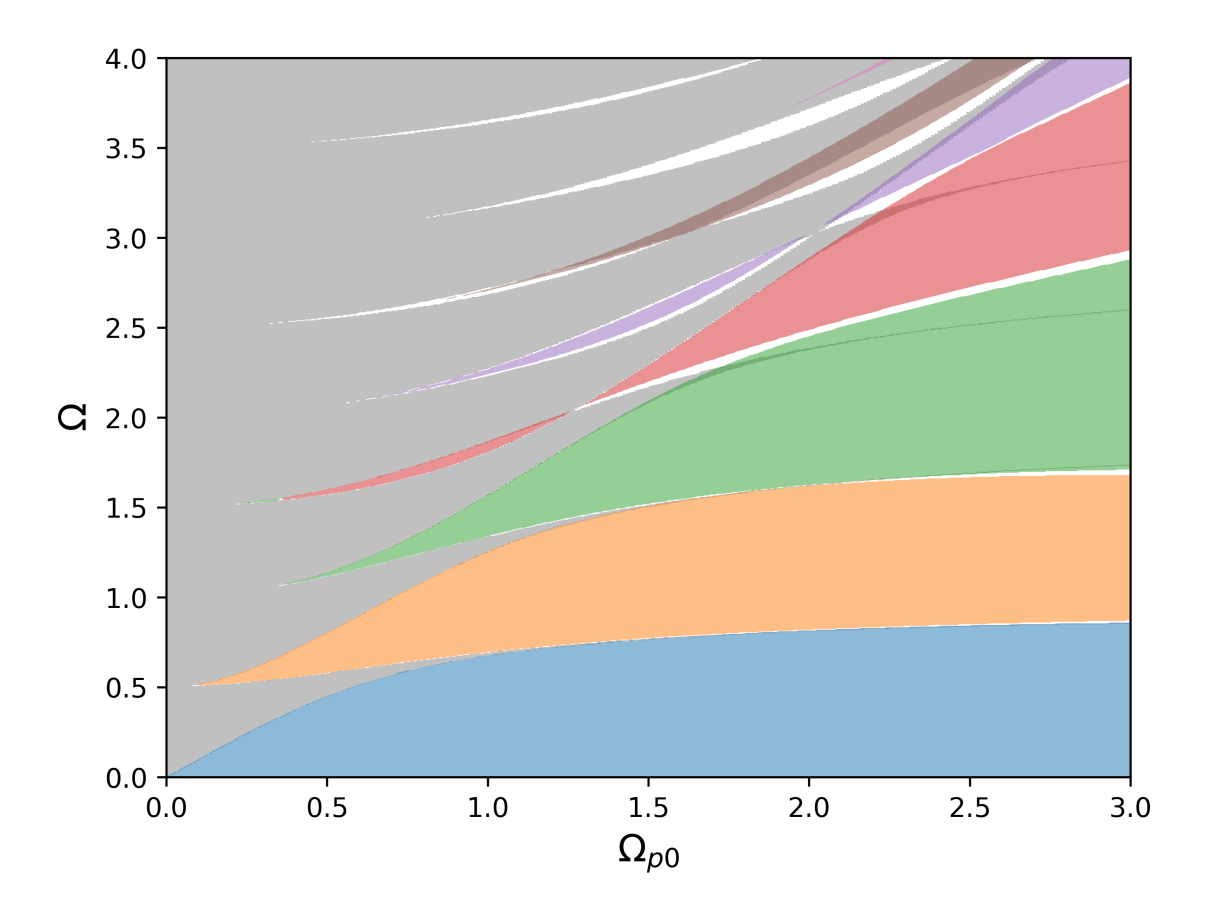


FIG. 10. The discontinuous density profile gap map (gray) is overlaid with predictions by the seven-mode reduced model for the cutoff region (blue), and bandgaps (orange, green, red, violet, brown, and pink). In contrast to the two-mode reduced model in Fig. 8, even bandgaps are present, and the odd bandgaps are less prominent. Forbidden islands appear in bandgaps three (red) and four (purple).

abrupt changes due to dielectric components or barriers. Given that the Fourier content of the density profile is the ultimate origin of bandgap features, choices can be made in advance to achieve desirable transmission characteristics. In cases where only the first bandgap is of interest, sinusoidal density profiles are sufficient. Where higher bandgaps are desired in order to target frequencies well beyond achievable lattice spacing and plasma frequencies, dielectric barriers or low fill fraction density profiles may be necessary in order to introduce higher Fourier content. This work also suggests that dielectric barriers can be introduced to achieve forbidden island like behavior, for example a band pass region that closes above a specified PPC average density.

Dissipative effects have not been included in this study, though they are likely to be non-

negligible in THz plasmas. Prior work on dissipation in both metallic and plasma PCs^{40,41} have shown that absorption of EM wave energy by a dissipative material peaks at frequencies with a slow group velocity. The physical interpretation is that slow moving waves have more time to interact and transfer energy than fast moving waves. As a result, increasing the electron relaxation rate does not lead to a change in the band structure per se, but does increase absorption around bandgap edges leading to the appearance of a wider bandgap in transmission spectra.

VII. CONCLUSIONS

PPCs have a smoothly varying density structure as compared to solid-state PCs which have discontinuous changes in material properties. A systematic understanding of the effect of smooth and discontinuous density profiles on transmission properties of PPCs is important to understanding and designing future PPC devices.

In this work, two one-dimensional density profiles are chosen that represent the limiting cases of smooth and discontinuous PPCs. Band diagrams are constructed for each assuming an unmagnetized, non-dissipative, cold plasma with stationary ions. Group velocity bandgap maps are then assembled from sets of band diagrams for a range of modulation amplitudes and lattice normalized plasma frequencies, and compared for both density profiles. The results are further examined through reduced models to elucidate the origins of major bandgap features.

Several general trends are identified. First, two profiles with the same lattice constant and average, maximum, and minimum densities can have different bandgap behavior. Second, the width of higher-order bandgaps is strongly correlated with density profile Fourier content. Stated more explicitly, the frequency and width of the *j*-th bandgap are a function of the lattice normalized plasma frequency and the magnitude of the *j*-th Fourier component. Third, high-order interactions of bandgaps can lead to complex effects like forbidden islands, where bandgaps open and close with increasing plasma frequency.

These results have interesting implications for the design of future PPC devices. The density profile shape becomes yet another parameter that can be tuned to achieve desired results. By designing the Fourier content of a density profile, through finer control of plasma shape or inserting solid components to create discontinuities, higher-order bandgaps can be directly controlled.

Group velocity bandgap maps prove to be a powerful technique in both PPC design and understanding the operating regime of a single device. While the system linearization technique used in this study to generate band diagrams is optimized for cold, un-magnetized, and non-dissipative plasmas, the group velocity bandgap map is agnostic to calculation method. Group velocity bandgap maps can either be generated directly for PPCs that include additional physics, or single band diagrams can be compared to these results for a deeper understanding in cases where computations are too costly.

This technique is also applicable to PPCs of higher dimensions. Work is already under way to study the transmission properties of two-dimensional PPCs with a variety of density profile shapes.

DATA AVAILABILITY

The data that support the findings of this study are available from the corresponding author upon reasonable request.

ACKNOWLEDGMENTS

The information, data, or work presented herein was funded in part by the Air Force Office of Scientific Research under Award Nos. FA9550-14-1-0317 and FA9550-15-1-0271. This material was also based upon work supported by the National Science Foundation under Grant No. PHY-2108419. This work was facilitated through the use of advanced computational, storage, and networking infrastructure provided by the Hyak supercomputer system at the University of Washington.

REFERENCES

- ¹L. Rayleigh, The London, Edinburgh, and Dublin Philosophical Magazine and Journal of Science **24**, 145 (1887).
- ²L. Rayleigh, The London, Edinburgh, and Dublin Philosophical Magazine and Journal of Science **26**, 256 (1888).
- ³E. Yablonovitch, Physical Review Letters **58**, 2059 (1987).
- ⁴S. John, Physical Review Letters **58**, 2486 (1987).
- ⁵E. Yablonovitch, T. J. Gmitter, and K. M. Leung, Physical Review Letters **67**, 2295 (1991).
- ⁶R. V. Nair and R. Vijaya, Progress in Quantum Electronics **34**, 89 (2010).

- ⁷J. Broeng, D. Mogilevstev, S. E. Barkou, and A. Bjarklev, Optical Fiber Technology **5**, 305 (1999).
- ⁸A. Salmanpour, S. Mohammadnejad, and A. Bahrami, Optical and Quantum Electronics **47**, 2249 (2015).
- ⁹H. Hojo and A. Mase, Journal of Plasma and Fusion Research **80**, 89 (2004).
- ¹⁰O. Sakai, T. Sakaguchi, Y. Ito, and K. Tachibana, Plasma Physics and Controlled Fusion **47**, B617 (2005).
- ¹¹O. Sakai, T. Sakaguchi, and K. Tachibana, Applied Physics Letters **87**, 1 (2005).
- ¹²B. Wang and M. A. Cappelli, Applied Physics Letters **107** (2015).
- ¹³B. Wang, R. Lee, R. Colon, and M. A. Cappelli, Microwave and Optical Technology Letters **59**, 3097 (2017).
- ¹⁴D. R. Biggs, A. Marcovati, and M. A. Cappelli, Journal of Physics D **52**, 055202 (2019).
- ¹⁵T. Sakaguchi, O. Sakai, and K. Tachibana, Journal of Applied Physics **101** (2007).
- ¹⁶B. Wang and M. A. Cappelli, Applied Physics Letters **108**, 161101 (2016).
- ¹⁷W. Fan, X. Zhang, and L. Dong, Physics of Plasmas **17**, 113501 (2010).
- ¹⁸Y. Wang, L. Dong, W. Liu, Y. He, and Y. Li, Physics of Plasmas **21**, 073505 (2014).
- ¹⁹A. M. Cook, J. S. Hummelt, M. A. Shapiro, and R. J. Temkin, Physics of Plasmas **20**, 043507 (2013).
- ²⁰G. Lehmann and K. H. Spatschek, Physical Review Letters **116**, 225002 (2016).
- ²¹G. Lehmann and K. H. Spatschek, Physics of Plasmas **24**, 056701 (2017).
- ²²J. Loverich and U. Shumlak, Physics of Plasmas 13, 082310 (2006).
- ²³A. Hakim and U. Shumlak, Physics of Plasmas **14**, 055911 (2007).
- ²⁴M. Lontano and N. Lunin, Journal of Plasma Physics **45**, 173 (1991).
- ²⁵M. Lontano and N. Lunin, Journal of Plasma Physics **48**, 209 (1992).
- ²⁶L. Qi, L. Shang, and S. Zhang, Physics of Plasmas **21**, 013501 (2014).
- ²⁷W. Chen, L. Yang, Z. Zheng, and P. Yu, in 2012 International Conference on Microwave and Millimeter Wave Technology (ICMMT), Vol. 3 (IEEE, 2012) pp. 843–846.
- ²⁸S. Prasad, V. Singh, and A. K. Singh, Progress In Electromagnetics Research M **21**, 211 (2011).
- ²⁹B. Guo and X.-M. Qiu, Optik **123**, 1390 (2012).
- ³⁰P. Drude, Annalen der Physik **306**, 566 (1900).
- ³¹P. Drude, Annalen der Physik **308**, 369 (1900).

- ³²F. Bloch, Über die Quantenmechanik der Elektronen in Kristallgittern, Ph.D. thesis, Universität Leipzig (1928).
- ³³B. Cockburn and C.-W. Shu, Mathematics of Computation **52**, 411 (1989).
- ³⁴U. Shumlak, R. Lilly, N. Reddell, E. Sousa, and B. Srinivasan, Computer Physics Communications **182**, 1767 (2011).
- ³⁵D. T. Prescott and N. V. Shuley, IEEE Microwave and Guided Wave Letters **4**, 352 (1994).
- ³⁶J. D. Joannopoulos, S. Johnson, J. N. Winn, and R. D. Meade, *Photonic crystals: molding the flow of light*, 2nd ed. (Princeton University Press, 2008) pp. 242–251.
- ³⁷V. A. Tolmachev, T. S. Perova, J. Ruttle, and E. V. Khokhlova, Journal of Applied Physics **104**, 033536 (2008).
- ³⁸J. M. Lourtioz, H. Benisty, V. Berger, J. M. Gérard, D. Maystre, A. Tchelnokov, and D. Pagnoux, Photonic Crystals: Towards Nanoscale Photonic Devices (Springer, 2005) pp. 1–514.
- ³⁹I. A. Sukhoivanov, I. V. Guryev, J. A. Andrade Lucio, E. Alvarado Mendez, M. Trejo-Duran, and M. Torres-Cisneros, Microelectronics Journal **39**, 685 (2008).
- ⁴⁰V. Kuzmiak and A. A. Maradudin, Physical Review B **55**, 7427 (1997).
- ⁴¹L. Qi, C. Li, G. Fang, and X. Gao, Plasma Science and Technology 17, 4 (2015).